Beamforming of Rayleigh and Love waves in the course of Atlantic cyclones

J. D. Pelaez Quiñones[1]*, D. Becker[1], C. Hadziioannou[1]

[1]Institute of Geophysics, University of Hamburg, Hamburg, Germany

Key Points:

- Primary and secondary microseismic Love and Rayleigh waves excited by Atlantic hurricanes were detected via onshore polarization beamforming
- The observed microseisms are only efficiently excited at certain shallow oceanic regions as the cyclone passes nearby
- Some signals are lasting and nearly source location-stationary, while others are transitory and originate behind the cyclone as it advances

*now at Géoazur, Campus Azur of CNRS, Sophia Antipolis, France

Corresponding author: Julián Pelaez Quiñones, julian.pelaez-quinones@studium.uni-hamburg.de/judape93@gmail.com

Abstract

The main sources of the ambient seismic wavefield in the microseismic frequency band (peaking in the ∼0.04-0.5 Hz range) are the earth's oceans, namely wind-driven surface gravity waves (SGW) coupling oscillations into the seafloor and the upper crust underneath. Cyclones (*e.g.* hurricanes, typhoons) and other atmospheric storms are efficient generators of high ocean waves with complex but distinct microseismic signatures. In this study, we perform a polarization (*i.e.* 3-component) beamforming analysis of microseismic (0.05-0.16 Hz) retrograde Rayleigh and Love waves during major Atlantic hurricanes using a virtual array of seismometers in North America. Oceanic hindcasts and meteorological data are used for comparison. No continuous generation of microseism along the hurricane track is observed but rather an intermittent signal generation at specific oceanic locations along the track. Both seismic surface wave types show clear cyclone-related microseismic signatures and are consistent with a colocated generation at near-coastal or shallow regions, however the Love wavefield is comparatively less coherent. We identify two different kind of signals: a) intermittent signals that originate with a constant spatial lag at the trail of the hurricanes and b) signals remaining highly stationary in direction of arrival even days after the hurricane passed the presumable source region. This high complexity highlights the need for further studies to unravel the interplay between site-dependent geophysical parameters and SGW forcing at depth, as well as the potential use of cyclone microseisms as passive natural sources.

Plain Language Summary

Ocean waves are responsible for the generation of microseisms, faint ground vibrations which have a rather complex character and which comprise a major portion of the background seismic noise of the earth. In this study, we implement a seismic detection method to study the microseisms generated by cyclones in the North Atlantic (hurricanes), which are major generators of large ocean waves. We observed that cyclones only seem to generate detectable microseisms as they move over certain regions in the ocean, namely near coastal or shallow water regions, and also that the apparent source regions of these microseisms are sometimes fixed while others move along with the hurricanes, trailing behind of them. Understanding the relationship between ocean waves and cyclone-related microseisms is an important step for the potential use of these vibrations to study the earth, ocean and atmosphere.

Keywords: *Ambient seismic noise, Oceanic microseisms, Hurricanes, Ocean gravity waves, Array seismology, Marine Geophysics*

1 Introduction

Atmospheric phenomena and ocean waves are long known to be intimately related, and the imprint of the latter in seismological records has been persistently pointed out (e.g. Gutenberg, 1936; Longuet-Higgins, 1950; Kibblewhite & Wu, 1996; Nishida, 2017). Water column pressure fluctuations induced by wind-forced surface gravity waves (SGW) and swells couple into the seafloor and produce elastic waves in the solid earth, so called *oceanic microseisms*. Evidence suggests that cyclones, have become increasingly stronger worldwide since the last four decades owing to global warming (Kossin et al., 2020); their latitude of formation and maximum magnitude is shifting polewards (Kossin et al., 2014); their built-up rate has sped-up (Emanuel, 2017b) and their associated rainfall volume increased (Emanuel, 2017a). The societal relevance of cyclones has thus grown accordingly at the same time that other effects of climate change such as sea-level rise make the scenario even more threatening. While cyclones have been traditionally a study subject for the meteorologist and oceanographer, understanding their dynamics and what to expect from them in the near future is of great interest for other fields as well. Con-

cretely, the analysis of microseisms have the potential of contributing to the understanding of the mechanical coupling between the atmosphere, ocean and solid earth.

Previous studies reported oceanic microseisms related to storms and hurricanes (both sub-types of cyclones) in different scenarios (e.g. Gilmore, 1947; Gutenberg, 1958; Sutton & Barstow, 1996; Gerstoft et al., 2006; Hadziioannou et al., 2012; Tanimoto & Valovcin, 2015). Oceanic microseisms are generally divided into primary (PM), having the same frequency as the causative SGW and being generated often close to the shore, and secondary (SM) with twice the frequency of the forcing SGW. Debate still exists on a set of matters, including the specific generation areas of these signals and the physical nature of the ocean-seafloor-subsurface coupling. Some authors argue that most microseismic energy originates near coasts in shallow waters (e.g. Essen et al., 2003; Traer et al., 2012; Bromirski et al., 2013; Ying et al., 2014), while others claim that teleseismic detection of microseisms in deep open waters is possible (e.g. Kedar et al., 2008; Landès et al., 2010; Meschede et al., 2017; Retailleau & Gualtieri, 2019). The forcing mechanism behind Love waves is still disputed: these are proposed to result from vertical water pressure interactions with sloping/irregular bathymetry (Saito, 2010; Fukao et al., 2010), horizontal tractions due to ocean wave movement (Ardhuin et al., 2015; Juretzek & Hadziioannou, 2017), or to a minor extent on conversions and multiple scattering (Ziane & Hadziioannou, 2019). A detailed knowledge on the shape and spectral characteristics of the cyclone-related microseismic sources, and their exact relation with the physical properties of the cyclones is still incomplete, although recent advances exist (e.g. Retailleau & Gualtieri, 2021).

The seismic array approach to study cyclones can be traced back to Cessaro and Chan (1989), who at the time used single-component $f-k$ beamforming to locate PM sources during the passage of two cyclones near the Pacific and Atlantic coasts of Canada with two land-based arrays, one in Alaska (with 19 stations) and the other inland Canada (25 stations). The authors concluded that the analysed signals (allegedly Rayleigh waves) had enough stability over one-hour windows to be useful for triangulation and that most energy came from near-shore processes that could be linked to the storms. No continuous tracking was sought by the authors and a broad area was triangulated. Later, Cessaro (1994) extended the study of Rayleigh waves into the SM band and included NORSAR as a third array in an attempt for continuous tracking. The author found that backazimuths do not follow the storm track directly. SM results are described as more stochastic, sporadically meandering around the synoptic region of peak SGW activity, while PM sources appeared more stable and localised, lying over specific near-shore regions in the Labrador sea and off the coast of western North America. Overall, the results of both studies had low space-time resolution but demonstrated that the seismic array detection of cyclones is possible. In contrast to these studies, the here implemented polarization beamforming processing as well as the use of modern seismic records allowed for the introduction of Love phase analysis and improved the achievable space-time resolution and coverage. In addition, the now available high resolution hindcast and cyclone meteorological data used in our analysis was not present for the former studies.

Later microseismic beamforming studies focused on regional ambient microseisms in Europe using pre-existing seismic arrays to resolve the dominant generation areas during longer time intervals, most of which appear to lie along coasts (e.g. Friedrich et al., 1998; Essen et al., 2003; Juretzek & Hadziioannou, 2017). Single-cyclone tracking was not the main aim of these studies but rather to define the dominant microseism spatial distribution over a given timespan. Friedrich et al. (1998) for example, used polarization beamforming at Graefenberg and NORSAR arrays to define a dominant source at the north-Norwegian coast. The Love/Rayleigh energy ratios in their study were found to be much higher for PM than for SM ambient noise, indicating possible differences in source mechanisms. Ward Neale et al. (2018) used the P-wave beamformer output of a number of arrays to produce a combined output image overlaid on a geographical grid.

According to the authors, their procedure sharpened and improved the coverage of the image in comparison to one single array. However, mixed results were found in terms of storm location, as some arrays failed to locate the storms under study. The sometimes large array-storm interdistances where quoted as a relevant factor for this.

The concrete goal of our study is to implement the polarizarion (3-component) beamforming method to analyse the seismic surface wavefield (Rayleigh and Love) during a few major north Atlantic cyclones (hurricanes) in the microseismic frequency band (∼0.05-0.16 Hz). In contrast to station configurations deliberately installed for array analysis (*e.g.* NORSAR, Graefenberg) we here utilize a virtual array consisting of onshore seismometer stations of the World-Wide Standardized Seismograph Netzwork (WWSN) originally installed for routine earthquake monitoring. The specific regions where the oceanic microseisms are generated is of particular importance, as some debate still exists on the topic. It is also sought to compare the spatio-temporal characteristics of the Rayleigh and Love wavefields, as several studies tend to consider only one of these wave types or body waves. We study the PM and SM wavefields in detail to relate them to the progression of the hurricane track and link their generation to specific areas and to outstanding meteorological and oceanographic characteristics. Generally speaking, we intend to contribute to the understanding of the complex relationship between atmospheric and seismic phenomena by gathering information on the ambient seismic wavefield during major hurricanes.

In the following sections, a short review on cyclones and microseisms as well as the applied data processing will be given. Then, we present the region of study alongside the utilized data and give beamforming results for selected hurricanes including a detailed discussion of these results. Finally, we summarize the most relevant observations and their implications.

2 Cyclones and microseisms

Cyclones are low-pressure center convective weather systems with well-defined structures and life-cycles that develop mostly over the ocean in the tropics and mid-latitudes, where warm waters are available. Depending on their maximum 1-minute sustained windspeeds, tropical cyclones (those that form almost exclusively in tropical regions) are referred to (in increasing order) as *tropical depressions*, *tropical storms*, *typhoons* (in the western pacific ocean) or *hurricanes* (in the eastern pacific and Atlantic ocean) (Wallace & Hobbs, 2006). When tropical cyclones move into medium or high latitude regions, these are denoted as: subtropical and extratropical, respectively. Cyclones are mostly clustered in the *tropical cyclone season*, during which the strongest ones occur. The Atlantic hurricane season peaks typically during the northern summer (between June and October). The center (*eye*) of cyclones usually has a radius between 10 and 60 km, while the whole systems have ROCIs (radius of the outermost closed isobar, a measure to define the radius of a cyclone up to its outermost wind circulation region) from about 200 km up to 1000 km. Their paths are often erratic, controlled by Coriolis effect and high-level winds but covering in average recurrent geographical corridors, translating roughly westward from the tropical Atlantic region where they form between the western tip of Africa and Middle America at about 2 to 10 m/s as they widen and intensify, and then shifting polewards to diffuse and weaken by cold waters or land along their path, to finally reach translational speeds of up to 25 m/s (Ochi, 2003).

Wind blowing over the sea surface is known to be the major cause for ocean surface gravity waves (SGW) at frequencies $\gtrsim 0.01$ Hz (Knauss (1997)) and their wave heights are proportional to the speed, timespan and fetch of the wind (Young, 1998). The strong winds of cyclones force the water surface to develop wind waves that later evolve into long-period swells as they radiate away more or less radially. The directional SGW spectrum of cyclones is rather complex, especially during landfall (Chen & Curcic, 2015). In

the northern hemisphere, the highest SGW tend to occur at the frontal sector (*i.e.* front left and right quadrants) of the cyclone (in travelling direction), near the area where wind-speeds are highest (Wallace & Hobbs, 2006; Esquivel-Trava et al., 2015). Because winds are a superposition of the forward motion of the storm and the circulating air, their intensity is the highest in the right (left) quadrants in the northern (southern) hemisphere. Farther away from the eye the SGW spectra become multimodal, consisting of a superposition of local wind-sea and swells (low frequency SGW after propagating large distances from their sources). Young (2006) explains that wave period is proportional to maximum wind speed (and thus wave propagation speed) and that swells originating near the intense wind crescent at an earlier point in the track dominate in all its quadrants except for the right-rear. Hu and Chen (2011) argue that the dominant wave direction in the front quadrants radiate out from the right of the eye, while in the rear are mostly locally generated, except for the rear left where outward radiation is also evident. Storm surges can also occur as cyclones approach coastal areas, where the wind-driven current can reach the shallow bottom, pushing water towards the coast and raising sea-level by several meters (Wallace & Hobbs, 2006).

The high amplitude SGW resulting from cyclones are believed to create two different types of ocean microseisms: The more energetic SM with twice the frequency of the generating SGW and the less energetic PM with the same frequency of the SGW. SM is commonly cited to be generated by non-linear wave-wave interactions between SGW of nearly the same frequencies travelling at quasi-opposite directions, which would result in standing SGW with amplitudes proportional to the product of the original waves, doubled frequencies (DF) and hydroacoustic waves that reach the ocean bottom travelling downwards nearly unattenuated (Longuet-Higgins, 1950; Hasselmann, 1963; Kibblewhite & Wu, 1996). Alternatively, it has been proposed that SM are caused directly by water column pressure propagation under Bernoulli's principle and via cylindrical wave radiation around the center of cyclones (Bowen et al. (2003)). SM have frequencies above $\sim$0.08 Hz in the open ocean and up to $\sim$1 Hz locally at marginal seas (Becker et al. (2020)), but tend to generate the strongest oceanic microseisms in the $\sim$0.1-0.2 Hz band. PM are thought to arise from ocean wave shoaling and SGW-seabed interactions over relatively shallow waters (Ebeling, 2012; Nishida, 2017). The typical frequencies of the latter in the ocean are in the range $\sim$0.05-0.1 Hz (10 to 20 s-periods).

3 Data

A total of six cyclones were selected for our study. These are summarized with their trajectories in Fig. 1. As every major hurricane develops its strength continuously, analysing the strongest ones has the advantage of containing lower categories at progressive stages. The categories, geographical paths, ocean depth ranges and inter-distances to array center were chosen to be as diverse as possible for comparison. Relatively simple and long trajectories were preferred to increase the probability of tracking.

3.1 Seismic data

A virtual array that we named "QC" near Saint Lawrence river in Quebec, Canada was arranged by selecting stations of the Canadian National Seismograph Network (CN) due to its proximity to the Atlantic coast and ideal aperture ($\sim$69 to 104 km, depending on missing stations). Fig. 2 shows its geometry and the array response function (ARF), *i.e.* its transfer function for two different frequencies. The ARF at 0.06 Hz (in the PM range) has a broad and prominent main lobe and a few weak side lobes, while that for 0.12 Hz (in the SM range) is more influenced by numerous side lobes while having a sharper central maximum. The latter is due to the mean inter-station distances (about 20 km), which lead to a minor degree of spatial aliasing of the shortest wavelengths without implicating our results. Station CN.CACQ of QC array was only available for hurricanes

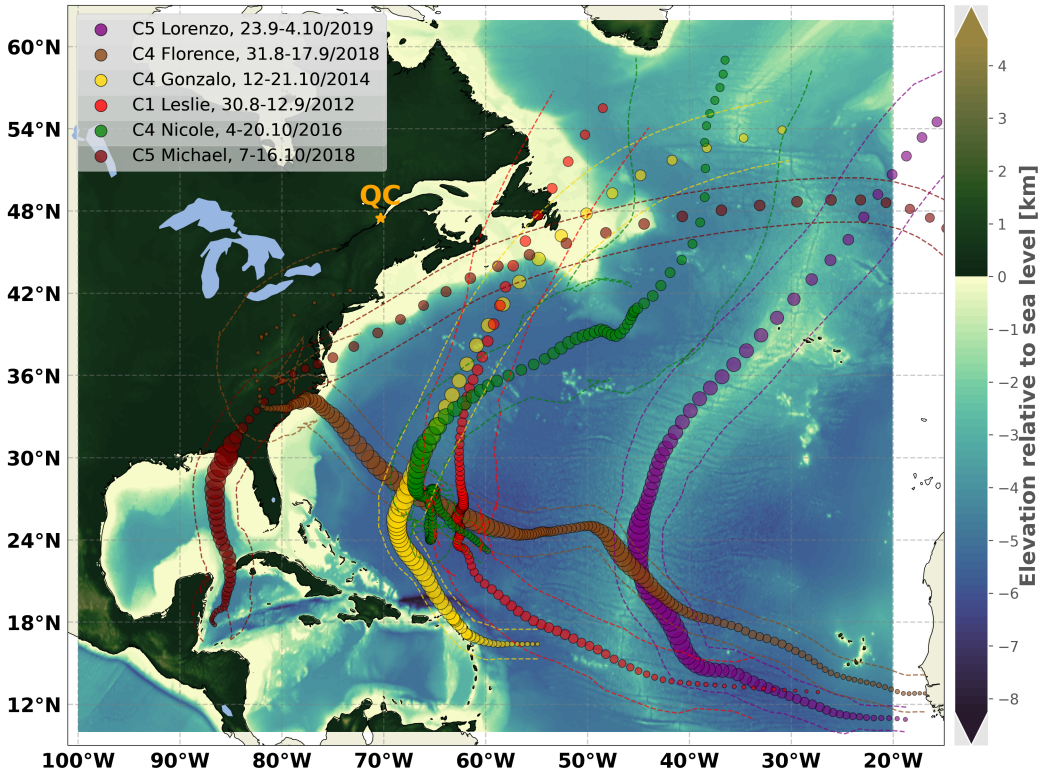

Figure 1. Atlantic hurricanes considered in this study. Categories on the Saffir-Simpson scale. Dots mark the locations of the *eye* of the hurricane at 3h-time steps. Their radius is proportional to the maximum sustained wind speeds (see Fig. 5 for absolute values), while the dashed lines mark the width (ROCI) of the system. The orange star marks the location of the QC array. Hurricane track data obtained from IBTrACS (Knapp et al., 2010).

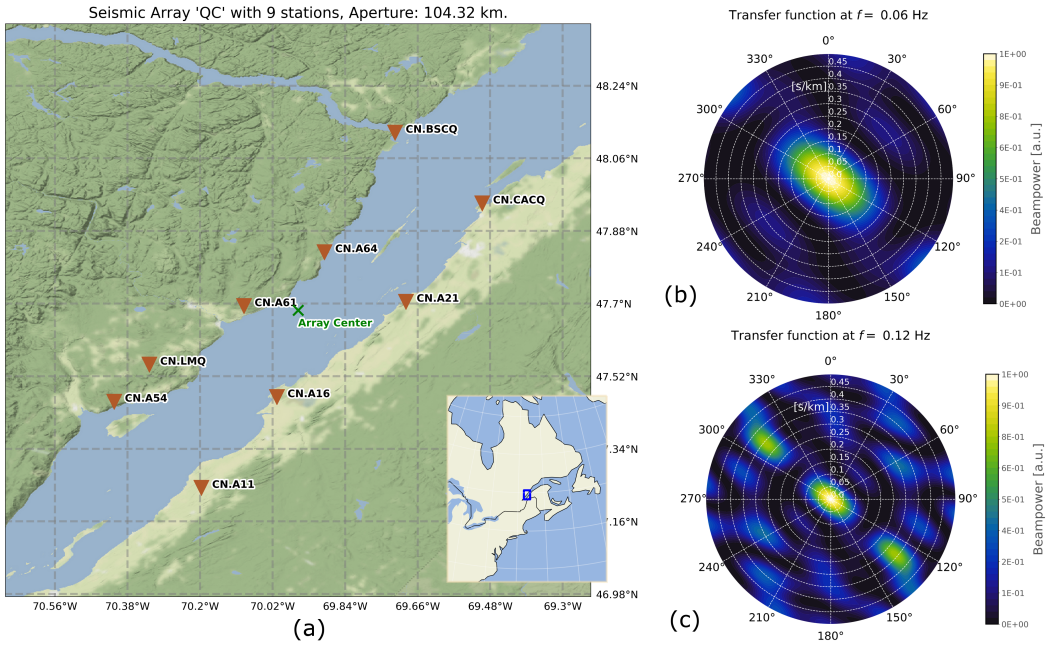

Figure 2. a) QC array geometry with inverted triangles indicating the seismic stations. The corresponding transfer functions (ARFs) are indicated for b) 0.06 Hz and c) 0.12 Hz. Stations CN.CACQ and CN.BSCQ are not taken into account for these ARFs, but doing so improves their quality (see text for explanation).

Florence, Michael and Lorenzo, while CN.BSCQ was missing for Gonzalo and Leslie. However the transfer functions were not substantially changed by adding or removing any of these two stations, remaining almost identical to those presented in Figs. 2b,c. On the other hand, the array lies in a seismically very quiet area and is relatively close to the Atlantic ocean. Further details on the arrays and data selection are given in the supplementary text S1.

3.2 Hindcast data

In order to compare the microseismic signatures with the ongoing distribution of ocean state anomalies, ocean hindcasts from a global model were used (see further details in Text S2, suporting information). The variables related to microseisms chosen for this study are:

- **Waveheight**: significant ocean wave height in metres. Represents the mean trough-to-crest amplitude of the highest waves in a region and is treated here as four times the standard deviation of the ocean surface elevation. It is expected to be proportional to the amplitudes of PM signals and partially to those of SM.
- **p2l (*or* F_{p3D}):** Power spectral density (PSD) (frequency spectrum) of the equivalent second-order SGW-induced pressure fluctuation near the water surface (F_p in eq. S1 in supporting information), which is a proxy for the strength of the nonlinear interaction of colliding SGW in opposite directions, and indirectly a proxy for the intensity of the associated SM signal with double frequency (DF) relative to the causative SGW (Stutzmann et al., 2012). This includes microseisms due to interaction of storm wind waves. The results are given in $\log_{10}(\mathrm{Pa^2 m^2 s} \times 10^{12})$. It empirically takes coastal reflections into account based on bathymetry and coastal

shape but other site effects at the source region are not considered (Gualtieri et al., 2021). To correct for this, the bathymetry amplification factors for land-measured microseismic Rayleigh waves for typical crustal parameters as proposed by Tanimoto (2013) are considered (See Text S3 for a detailed description of this variable as here implemented).

4 Methods and data processing

4.1 Polarization Beamforming

We use polarization beamforming, *i.e* three-component beamforming (Esmersoy et al., 1985; Löer et al., 2018; Nakata et al., 2019) to determine the Love and Rayleigh waves contributions in the incoming microseismic wave field at our virtual network. The goal of beamforming is to separate the coherent portion of the recorded wavefield from the stochastic one. This is done by generating outputs (*beams*) with the largest possible signal-to-noise ratio (S/N), which (in the time domain) are propagation model-dependent stacks of lagged input traces or equivalently (in the frequency domain) the weighted linear superposition of Fourier transforms of the cross-correlation between every pair of recordings, as here implemented. If coherent and prominent signals exist, the suitable set of weights among a space of possible combinations increases the output power, *i.e.* the *beampower* (BP), which in turn remains comparatively low if uncorrelated noise dominates. BP can be expressed in the frequency (f) domain as (Nakata et al., 2019):

$$BP(f) = \frac{1}{L^2 M^2}\mathbf{w}^H \mathbf{X}(f)\mathbf{X}^H(f)\mathbf{w} = \frac{1}{M^2}\mathbf{w}^H \mathbf{C}(f)\mathbf{w}, \tag{1}$$

where H denotes a conjugate transpose, L is the number of samples, M the number of sensors and $\mathbf{X}(f)$ contains the Fourier transform of each recording. The entries in $\mathbf{w}$ are the so-called weights that maximise BP depending on the assumed wave type (*e.g.* polarization state and wavelength) as well as the array geometry. The term $\mathbf{C}(f)$ is known as the cross spectral density matrix and can be though of as the kernel of beamforming, having information on the phase-delay relations between every pair of spectra from any two sensors, namely the Fourier transform of the auto/cross-correlation between every pair of stations.

BP can be regarded as a measure of the relative coherency and implicitly the amplitude of the signal traveling through an array. Coherency refers in our context to the degree of agreement/predictability of a signal under a particular propagation model, or alternatively, as the degree of certainty to relate the signal to a unique source acting at a defined location and over a given timespan. In the approach used here, a single, plane wave front will produce a high BP value while several interfering sources or bent wave fronts would result in lower BP values. For details on the implementation of beamforming see the supplementary Text S4.

4.2 Seismic Data Processing

After pre-processing of the raw data (see Text S5 in the supporting information for details), the polarization beamforming was implemented using the approach outlined in Esmersoy et al. (1985) and developed by Juretzek and Hadziioannou (2016), in which a grid-search in the f-domain is performed using the cross spectral density matrix. A plane-wave is assumed and thus anisotropy and wavefront curvature are ignored. This is normally a safe assumption for the far-field and for wavelengths in the order of the aperture of the array.

For beamforming, we investigate two polarization states of the microseismic wavefield: elliptic retrograde and transverse, representing retrograde Rayleigh waves and Love

waves, respectively. We set the slowness range to 0.22-0.37 s/km in order to include only surface waves and exclude most of the body wave energy or other undesired phases. The beamforming analysis window length (T_{BF}) was set to 300 s with a 50% overlap of consecutive windows, and the covariance matrix was averaged over 24 time windows, so that the output snapshots have a 1-hour resolution, unless otherwise specified. Performance tests to detect earthquakes of magnitude as low as 5.0 were successful. However a typical backazimuth (β) deviation of $\pm 5^\circ$ was observed, so that this is taken as the implicit uncertainty of our estimates.

5 Results

In the following, the polarization beamforming results for two hurricanes (C1 Leslie in 2012 and the last four days of C4 Gonzalo in 2014, see Fig. 1) at PM and SM frequencies are illustrated in detail as a way of example. Thereafter, summarized results for all the hurricanes considered are explained.

5.1 Leslie and Gonzalo - Primary microseisms

Z-component spectrograms recorded at a station CN.LMQ of the QC array during hurricanes Leslie (Fig. 3a) and Gonzalo (Fig. 3b) depict intermittent energy pulses with variable duration and frequency distribution. A lobe of relatively continuous PM energy below 0.1 Hz is observed during the last stages of Leslie (indicated by a black circle). The double-frequency (DF) phenomenon is particularly clear during Gonzalo, as the low-frequency PM features repeat themselves with stronger amplitudes and twice the frequencies in the SM range between the 17-20th of October. The linear trends during the dissipation stage (black segments) approximate the dispersion of prominent microseismic arrivals, which are typical for storms approaching. Based on the short (deep water) linear SGW group velocity dispersion relation ($U_g = g/4\pi f$) as in Bromirski and Duennebier (2002), a distance (Δx) from the SGW source (any region under the cyclone) to the microseismic source region can be roughly estimated from the slopes of these linear trends ($\Delta f/\Delta t$) by using:

$$\Delta x = \frac{g}{4\pi}\frac{\Delta t}{\Delta f} \tag{2}$$

where g is the acceleration of gravity at sea level and t represents time. This yields an estimated distance in the range 600 to 1000 km, which is somewhat above the average radius of these hurricanes during dissipation stage ($\sim$450 km). Figs. 3c-f show the maximum BP values in the time-backazimuth (t, β) space picked over the slowness range for each time and azimuthal step. The BP was pre-averaged at each slowness step in the PM frequency band (0.05-0.09Hz). The features in the spectrograms partially match those in the beamforming results for both Rayleigh (Figs. 3c-d) and Love (Figs. 3e-f) waves during Leslie (left column) and Gonzalo (right column). The colored dots depict the true bearing towards the center of the investigated hurricane and the black dashed lines its outermost winds from the perspective of the QC array, respectively. White dots represents the global and most prominent local BP maxima for each time step.

Based on Figs. 3c-f, a set of observations can be pointed out: 1) two types of apparent sources of the BP signatures stand out that can be related in time and space to the tracks of the main hurricanes: stationary (*i.e.* static, displaying constant backazimuths, see September 2-11 during Leslie and October 17-19 during Gonzalo) and non-stationary (*i.e.* moving and radiating signals continuously changing in direction of arrival, see September 11-13 during Leslie and October 19-20 during Gonzalo); 2) Both signals can be associated with sections of the hurricane tracks remarkably well, the former appearing as the hurricane intercepts the 160$\sim$165° backazimuth range in both cases and remaining

active for a couple of days after the true hurricane backazimuth significantly changes, while the non-stationary signals have a noticeable spatial shift looking towards the rear rim of the hurricane as it moves northwards. This is particularly clear for both Rayleigh and Love waves during Gonzalo (Figs. 3d,f); 3) While the BP maxima are aligned with the hurricanes considered, no clear correlation exists for the simultaneously active cyclones (light blue-colored dots in Figs. 3c,e) occurring farther away ($\gtrsim$ 4000 km) in the ocean, so that their contribution to the total BP is negligible; 4) Rayleigh and Love waves are both generated by the hurricane at about the same time arriving from about the same direction, while having different coherency levels (absolute BP values are generally higher for Rayleigh waves and have thus a higher contrast with respect to the background levels) and statistical variations in time and space distributions (Rayleigh maxima tend to be less scattered than Love wave maxima).

Consistent with the first observation, it can be hypothesised that the stationary signals are related to fixed regions in the ocean that are "activated" as the hurricane passes nearby and remain active for some days after it moves away. On the other hand, the non-stationary microseismic sources trail behind the hurricane and can be detected as it approaches the coast closest to the array. This can be observed through comparison with the mean and maximum significant waveheights over a 4×4 degs-square centered at Bermuda island in the Sargasso sea and the Gulf of Maine near the US-Canada border (Fig. 3g,h), both being likely locations for microseism generation as these are the shallowest and most bathymetrically variable oceanic regions lying simultaneously closest to the QC array and along the observed stationary microseismic backazimuth line (160∼165°). The waveheights at the Gulf of Maine remain relatively low and stable during the passage of both hurricanes, while those at Bermuda increase by several meters correlating with the onset of the stationary PM signal. However, it is also observed that the microseismic signals continue to be generated at the same location even after the waveheights decay, such that a third source location centered elsewhere along the stationary backazimuth line might exist. Based on the assumption that PM is generated by the largest wave heights, an expected azimuthal distribution of sources can be obtained from the waveheight hindcasts (Figs. 3i-j) which shows a partial agreement between the seismic and the hindcast data, as high waveheights occur beneath the hurricane track, as expected. However, according to the hindcast model the maximum waveheights occur approximately under the eye of the cyclone and not in the rear quadrants as the seismic data suggest, while at the same time not all the BP features are clearly represented in the hindcast data and vice-versa.

5.2 Leslie and Gonzalo - Secondary microseisms

Apart from statistical backazimuth variations, the source distribution of SM (in the band 0.10-0.16 Hz) Rayleigh and Love waves are comparable (Figs. 4a-d), although a few arrivals of one wave type are occasionally not evidenced in the other. The stationary and non-stationary signatures are still evident for both hurricanes and are similar to those of PM, yet there appears to exist a noticeable variability in direction of arrival of the main hurricane microseisms, being slightly higher for SM in comparison to PM. The F_{p3D} variable is shown here for comparison instead of waveheights, as SM are expected to result from non-linear SGW interactions. Similarly to the waveheights and the corresponding PM results, higher F_{p3D} values are observed at Bermuda as the stationary signals occur in comparison to the Gulf of Maine (Figs. 4e-f), while the F_{p3D} values in the latter increase during the very last days as the hurricanes approach the Grand banks off Newfoundland. The azimuthal distribution of F_{p3D} (Figs. 4g-h) shows a more scattered distribution of sources which is consistent with the higher variability of maxima in Figs. 4a-d. A good consistency between the hurricane tracks and the maximum F_{p3D} values exists, as they overlap each other while the stationary microseismic signal occurs (Sep. 4-11 for Leslie and Oct. 17-18 for Gonzalo in Figs. 4g,h). Here however, a noticeable backazimuth lag between the eye of the hurricane and the maximum F_{p3D}

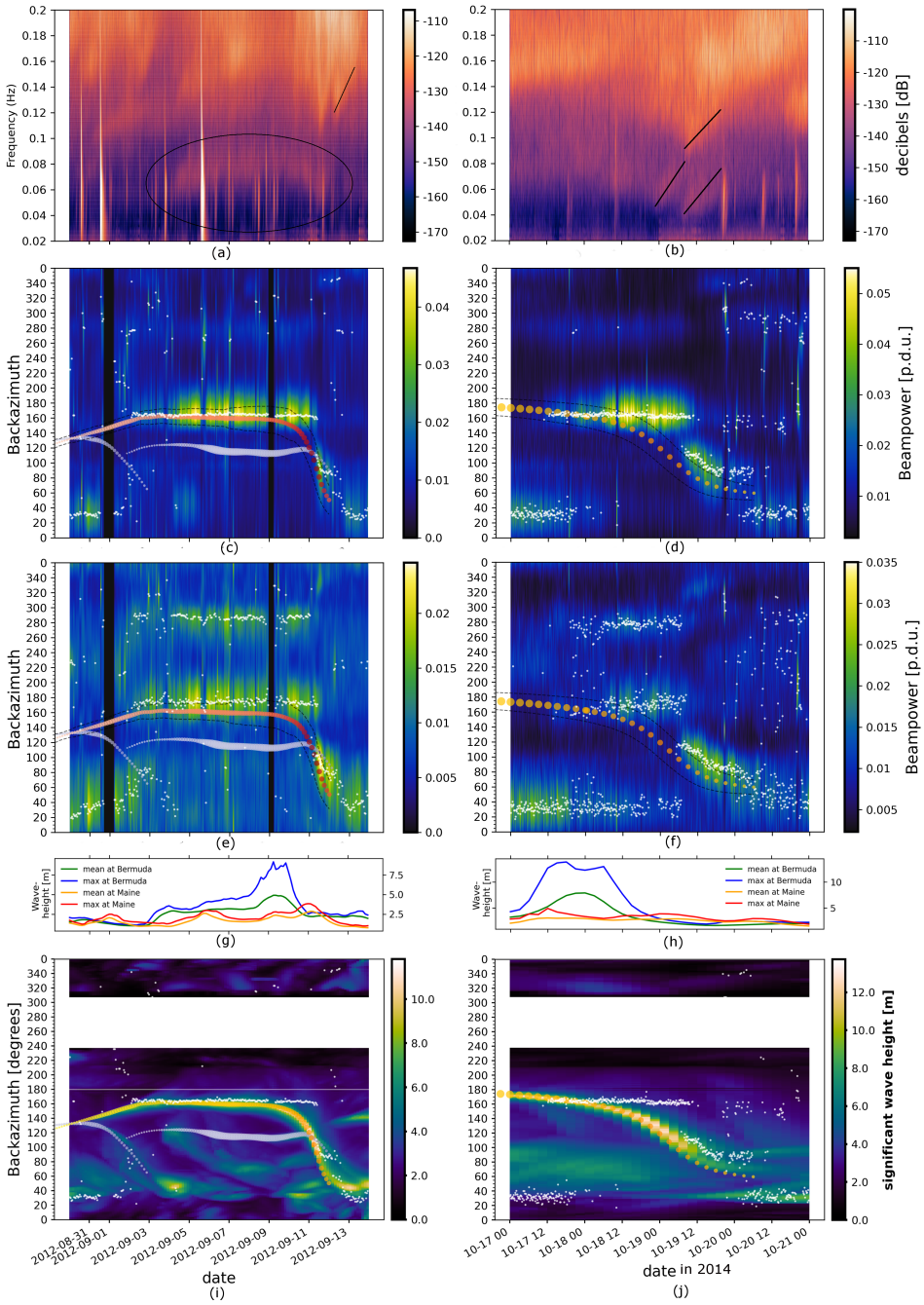

Figure 3. Results for Leslie (left column) and Gonzalo (right column) in the PM band (0.05-0.09 Hz). a,b) Spectrograms with 256s-PSD time window and 60% overlap. BP as a function of time and backazimuth at QC array for Rayleigh (c,d) and Love (e,f) waves. True bearings at regular time steps towards the eyes of Leslie (Gonzalo) are shown as red (orange) dots (their saturation is proportional to maximum sustained windspeeds), while the backazimuth towards the cyclone rims (ROCI) are marked by the dashed black lines. Simultaneous hurricanes located farther away are shown as blue dots. The mean and maximum significant waveheights over a 4×4 earth degs-square centered at Bermuda and the Gulf of Maine (g,h) and the maximum waveheights observed along 4000km-radius lines away from the QC array (i,j) are shown for comparison overlaid by the same Rayleigh BP maxima of (b,c) respectively as white dots.

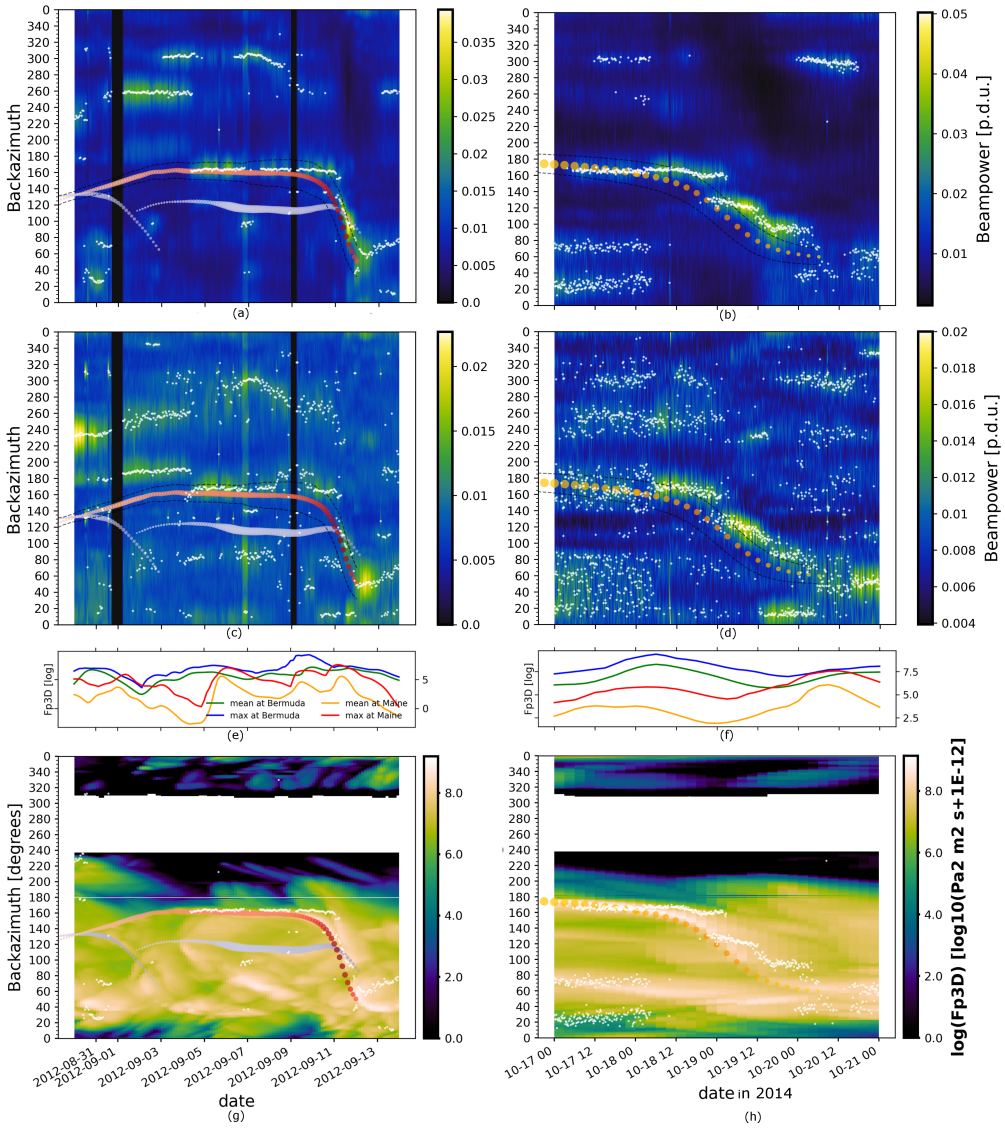

Figure 4. Results for Leslie (left column) and Gonzalo (right column) in the SM band (0.10-0.16 Hz) following the scheme of Fig. 3. BP as a function of time at QC array for Rayleigh (a,b) and Love (c,d) waves. The (logarithmic) mean and maximum F_{p3D} values in 4×4 degs-square surfaces at Bermuda and the Gulf of Maine are shown for comparison (e,f). The maximum F_{p3D} values observed within a distance of 4000km in the respective azimuthal direction from QC array (g,h) are shown for comparison, overlaid by the same Rayleigh BP maxima of (a,b) as white dots.

values exists during the last days of both hurricanes, at the same time that the non-stationary BP signature is observed (white dots in same figures).

5.3 Temporal and azimuthal distribution of hurricane microseisms

In order to visualize the temporal distribution of BP signatures for all the hurricanes considered, Fig. 5 summarizes the BP values (colour coded) and the degree of agreement between observed/expected backazimuths, calculated as $\beta_0/(\Delta\beta+1)$, *i.e.* the inverse of the deviation between the (true) backazimuth towards the eye of each hurricane

and that of the global BP maximúm for PM at each time step ($\Delta\beta$) using $\beta_0 = 4°$ as a reference normalization value for all hurricanes, so that backazimuth matches of this order or less are exaggerated. Rayleigh waves (Fig. 5a) show higher BP values than Love waves (Fig. 5b), which could be explained as a higher coherency of the wavefield of the former (or lower S/N ratio of the two-component transversal polarizations). The results for SM are similar in distribution but on average much lower in absolute BP values. The latter are included in the supplementary material (Fig. S1 in supporting information).

From Fig. 5 it can be observed that in overall no clear correlation exists between the hurricane category and the degree of observed track agreement. Particularly, hurricanes Gonzalo, Nicole and Lorenzo do not show a good correlation, while Florence and Michael only show partial correlation for a few days. Hurricane Leslie has high levels of backazimuth agreement along its lifetime, but the category variations are not clearly reflected in its seismic response. Moreover, this agreement is only apparent from the perspective of a single array. The highest BP values do not necessarily match timespans with the highest observed/expected backazimuth agreement nor with those having the highest hurricane category. Figs. 5a-b indicate a low agreement in azimuthal directions as obtained from BP maxima and the the meteorological centre of the hurricane during closest approach to the array, which is explained by the fact that the detected signals often point towards the trail of the hurricane, as discussed in Secs. 5.1 and 5.2. However, high Rayleigh wave BP values tend to occur shortly before and during the closest hurricane approach (Fig. 5a), indicating reliable signals. This is not as obvious for Love waves however (Fig. 5b). The higher coherency of PM Rayleigh waves than Love waves might be due to the fact that there is generally less incoherent Rayleigh wave energy in this frequency band and the large deviation at the closest hurricane approach to the array could correspond to the fact that the signals are not generated at the centre of the hurricane but at some other region of it. It is also worth noting that low track agreements where the smallest inter-distances exist do not necessarily indicate bad correlations, having in mind that large objects cover a wider range of backazimuths the closer they are to the observation point. In general, it is confirmed from Fig. 5 that coherent microseismic signals likely related to hurricanes only occur intermittently and not during their whole trajectory.

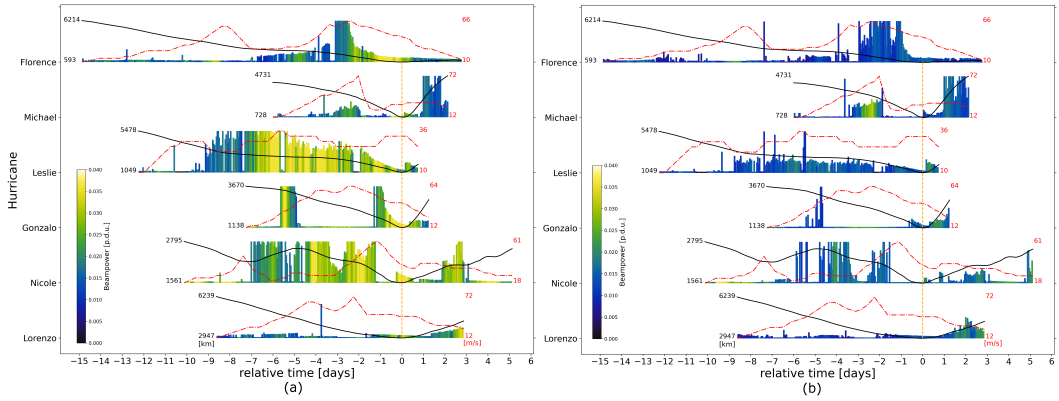

Figure 5. Track agreement between expected/observed backazimuths of the BP maxima relative to the bearing towards the eye of each hurricane (as the height of each bar - see text for detailed description) for Rayleigh (left) and Love (right) waves in the PM band. Data is aligned relative to the closest approach of each hurricane to the QC array (vertical orange lines). Distances between the array and hurricane center as continuous (black) lines and maximum sustained wind speeds in (red) dotted-dashed line. The values of largest and smallest distances (maximum windspeeds) during study the interval are given to the left (right)

The maximum BP value in each azimuthal direction along the entire lifetime of each hurricane (global BP maxima of beamforming plots as those of Figs. 3c,d,e,f and 3a,b,c,d) are depicted in Fig. 6. For PM (Figs. 6a,c), well-defined BP maxima with backazimuths towards the Atlantic ocean stand out for hurricanes Leslie and Gonzalo (marked in dashed black lines) as well as for most hurricanes on both Rayleigh and Love waves. In particular, the $\sim 165°$ direction belonging to the stationary signal tentatively linked to Bermuda island described for Gonzalo and Leslie in Secs. 5.1 and 5.2 is also present for the remaining hurricanes and for both, Rayleigh and Love waves. Recurrent signals at $30-60°$ occur likewise during each hurricane. Other representative backazimuths only exist for some of the hurricanes, but some dominant directions are clearly discernible.

SM maxima (Figs. 6b,d) exhibit a higher spatial variability, but still dominant backazimuths also occur that barely match between Rayleigh and Love waves. Notice that the BP value range (in blue) is considerably smaller for the latter in comparison to former, implying that Love waves have BP values that are closer to the noise floor and are thus more likely to be affected by random fluctuations. This observation applies as well for the (low) BP values of some hurricanes relative to others (*e.g.* Florence and Michael relaative to the others).

It follows from Fig. 6 that the surface wave microseisms that occur during major hurricanes are bounded to some fixed directions. This is particularly clear for PM, while at the same time a higher azimuthal variability exists for SM, in accordance with the fact that the latter could theoretically be generated over a larger set of oceanic regions, and not only near the coast, as expected for PM. Rayleigh wave signals are more stable and consistent with specific directions of arrival in comparison to Love waves for both the PM and SM bands.

The maps in Fig. 7 synthesise the observations in Figs 5 and 6 for hurricanes Leslie (Figs. 7a,c) and Gonzalo (Figs. 7b,d) and additionally depict hindcast data averaged over the timespan of the hurricanes. Large significant waveheights (Figs. 7a,b) at or near coastal/shallow waters indicate regions where efficient PM generation is expected, while large F_{p3D} values (Figs. 7c,d) are in principle expected where the strongest SM are excited. The tracks of the hurricanes are partially observed as aligned maxima in the hindcast data and the higher variability of SM sources in comparison to PM observed in Figs. 6b and 6d is also apparent in the F_{p3D} maps in comparison to the waveheights.

The backazimuths corresponding to the BP maxima in Fig. 6 are shown in Fig. 7 with a $5°$ uncertainty range. These backazimuths show a rather low correspondence with regions where the maximum waveheights (or F_{p3D}) occur. In fact, some of the beamforming maxima point towards regions with low mean oceanic anomaly along distances of more than 4000 km. Apart from the continental platform of North America, islands and seamounts in the Sargasso sea and the Caribbean, most ocean depths in the western North Atlantic exceed 4 km (Fig. 1), which can be a factor for preventing the excitation of sufficiently strong microseisms. Conversely, some of the regions with high SGW anomaly are not represented in the beamforming analyses, which would only be consistent for weak teleseismic sources or exceedingly deep waters in the case of PM but not otherwise. On the other hand, some of the observed seismic sources do match locations where high wave heights and F_{p3D} values occur, *e.g* the $\sim 52°$ and $\sim 98°$ backazimuths crossing the Labrador sea and the Grand banks of Newfoundland, respectively, during Leslie, or the stationary signal at $\sim 168°$ near the Sargasso sea. As discussed in 5.1 and 5.2, it is confirmed that the most likely location of the stationary source along the $\sim 165°$ backazimuth line is somewhere near Bermuda island, where high waveheights as well as F_{p3D} anomalies occur as opposed to the Gulf of Maine, which is the closest shoreline along that line but has very low mean SGW amplitudes.

In summary, our beamforming results indicate that cyclone-related microseismic signals are only excited at particular backazimuths roughly sourced towards the loca-

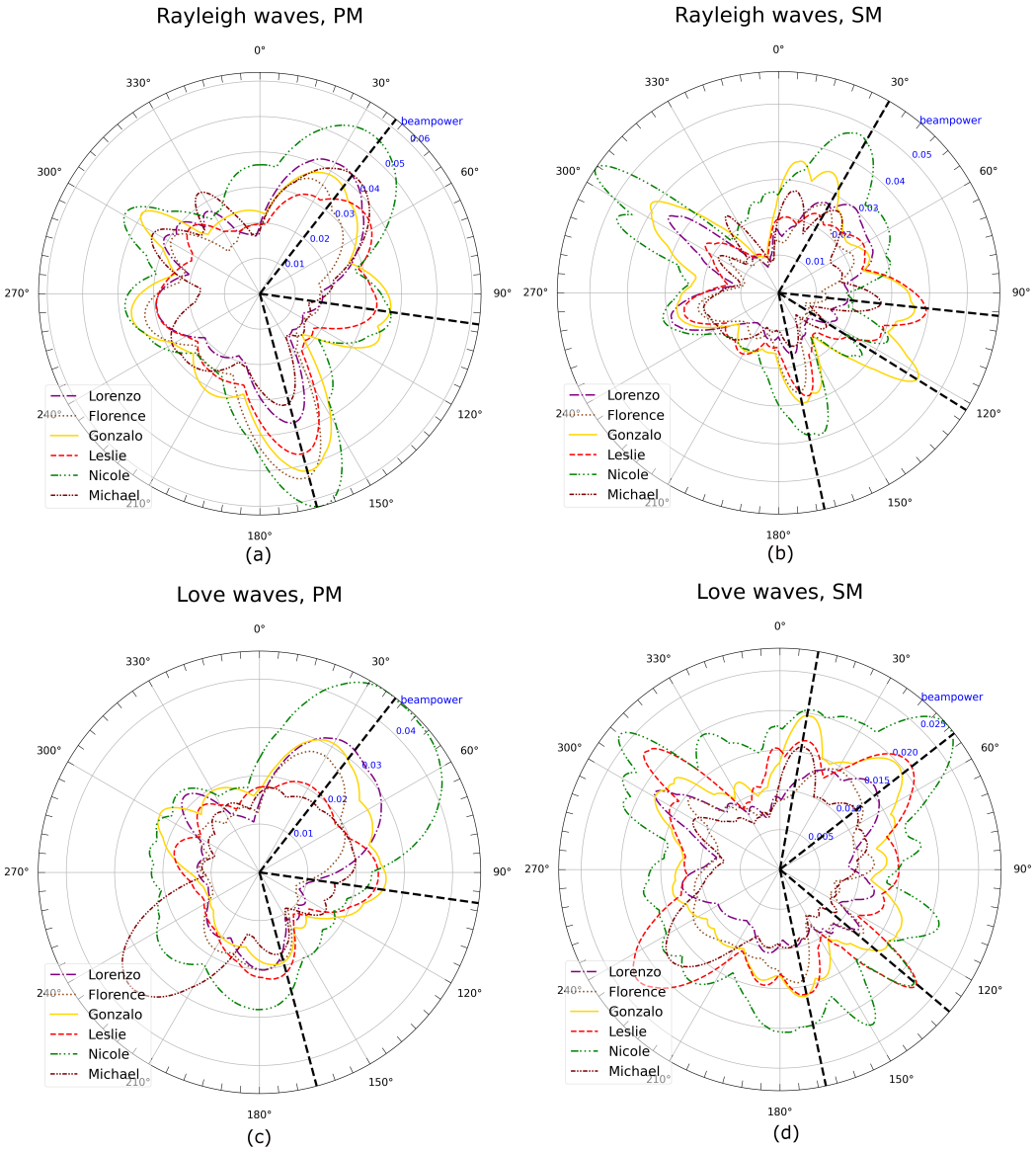

Figure 6. Azimuthal distribution of maximum BP values (at each backazimuth) during the lifetime of each hurricane after averaging over the corresponding frequency range in the PM (a,c) and SM (b,d) bands. Results are given for Rayleigh and Love waves (upper and lower row, respectively). Some of the most prominent arrivals for Leslie and Gonzalo (and also for the remaining hurricanes) looking towards the Atlantic ocean marked in black dashed lines.

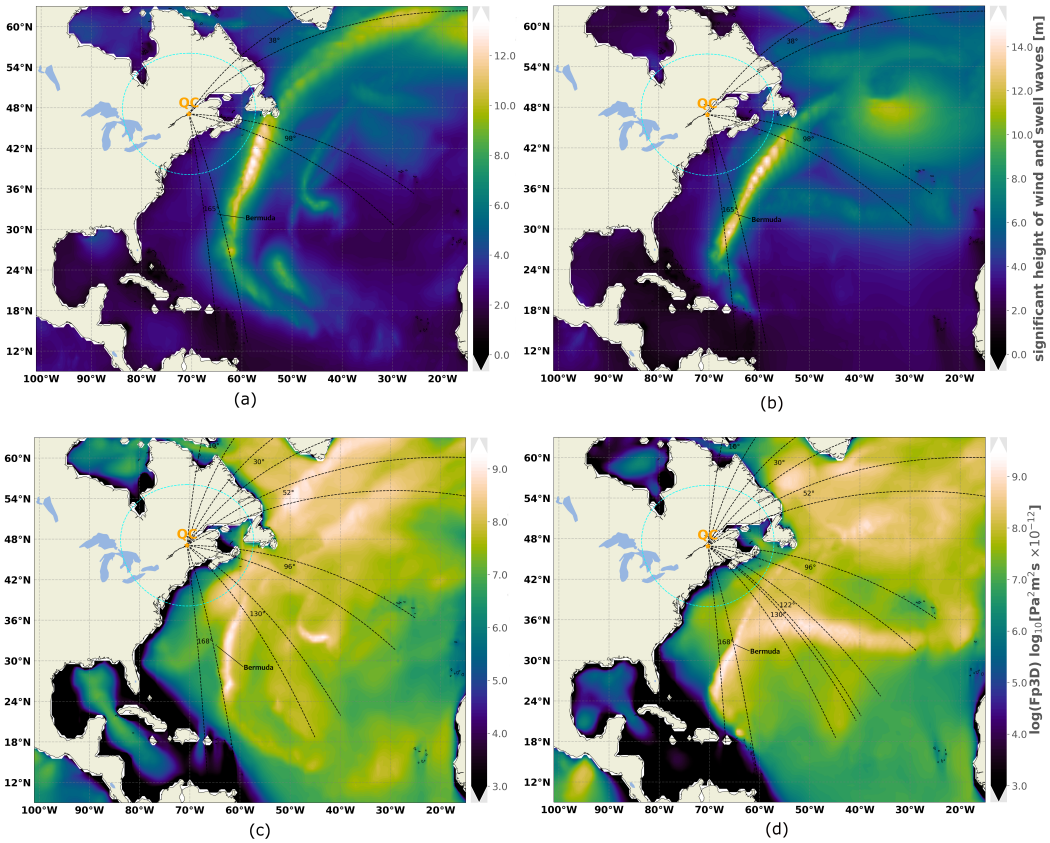

Figure 7. Significant waveheights (a,b) and F_{p3D} (c,d) maps for Leslie (a,c) and Gonzalo (b,d) with the prominent directions of arrival of Fig. 6 represented in ±5°-sectors and 4000 km-long lines (black dashed). For scale reference, a 1000 km-radius around the QC array is shown in cyan (comparable to the maximum distance found in 5.1).

tion of the corresponding cyclone, as if microseism generation regions were "activated" by the latter. Fig. 8 depicts a full-year beamforming analysis at QC array. It can be seen that particularly for Rayleigh waves (Fig. 8a) consistent directions of arrival occur throughout the whole year and not only between June and October, which corresponds to the north Atlantic hurricane season. For instance, the $\sim 165°$ stationary microseismic source observed for several hurricanes and outlined in Figs. 6a,c is most active during the northern hemispheric summer, but also remains active and stable at other times of the year. The same applies for other backazimuth ranges where beampower (BP) maxima tend to cluster. Similarly, the $\sim 38°$ source is most active during the northern hemispheric winter season, while the $\sim 98°$ source pointing towards Newfoundland is only sporadically active throughout the year for no more than a couple of days in a row. The Love wave BP maxima (Fig. 8b) are more scattered, variable and often do not match the direction of arrival of those for Rayleigh waves, but the general picture and the seasonal variations remain the same. The $\sim$ 38° and $\sim$ 165° stationary sources can be traced for Love waves, having relatively low continuity throughout the year.

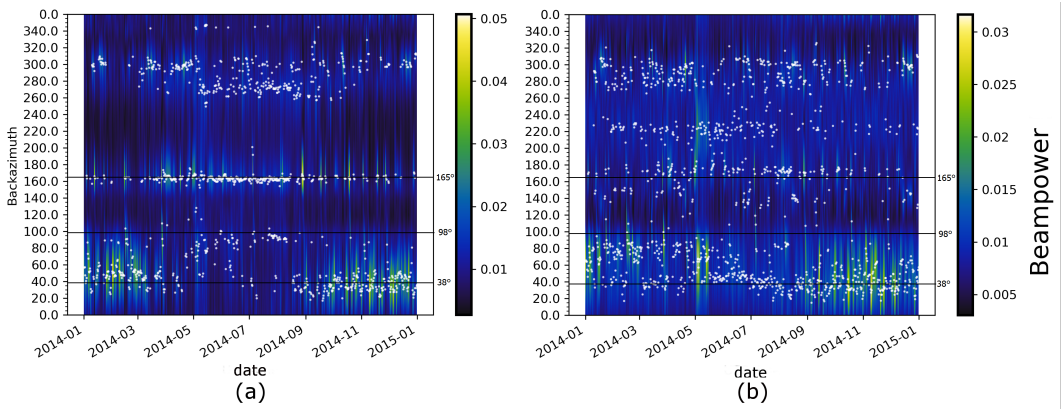

Figure 8. Backazimuth versus time plot for primary microseisms (PM) in 2014 averaged at 1-day timesteps for Rayleigh (a) and Love (b) waves. The dominant PM backazimuths of Figs. 6a,c are marked for comparison. White dots represent prominent BP peaks.

6 Discussion

We observe hurricane generated Rayleigh and Love waves microseisms originating from the North Atlantic at a virtual seismometer array in Canada in both the PM and SM bands. These microseisms manifest as semi-continuous but intermittent pulses prone to fall under the detection threshold if sufficiently weak or at very large source-station separations, preventing a continuous detection and thus continuous cyclone tracking via far-field arrays.

Our results argue in favour of nearly colocated sources of cyclone-related microseisms for Love and Rayleigh in both PM and SM bands, suggesting common forcing mechanisms and/or a strong site control. This observation is supported by e.g. Nishida et al. (2008); Juretzek and Hadziioannou (2016, 2017). Matsuzawa et al. (2012) conclude that moderate deviations exist between the Rayleigh and Love wavefields source areas, while acknowledging that the arrival directions of both are similar. Gal et al. (2017) investigated the background microseismic Rayleigh and Love wavefield in the high frequency end of SM (0.35 - 1 Hz) and observed a markedly distinct spectral and azimuthal distribution of each, Love waves correlating with near-continent sedimentary basins while Rayleigh waves correlate with convex coastlines. The source area colocation for both PM

and SM is also pointed out by e.g. Cessaro (1994) and Nishida et al. (2008), while several studies argue that PMs are only linked to shallow areas, while SMs can be generated in the deep ocean as well, as mentioned in Sec. 1. We note however, that the background microseismic wavefield resulting from swells and wind regimes acting over broader oceanic regions and longer time scales could differ from the microseismic wavefield linked to the more spatially localized and short-lived cyclone winds and their corresponding highly directional swells.

In spite of the aforementioned, the observed backazimuths of Love wave BP maxima in Figs 3 and 4 tend to have a higher variance and less continuity than those of Rayleigh waves, as the latter have smoother, less scattered and in general less diffuse cyclone-related signatures. This is in agreement with a Love wavefield generated over a comparatively broader generation area or resulting from complex radiation patterns due to a strong influence of heterogeneities and/or propagation effects. Previous works have explained this observation in terms of shear tractions due to ocean wave-induced pressure fluctuations over seabed topographic features (Fukao et al., 2010), scattering, wave conversions and diffractions (Juretzek & Hadziioannou, 2017; Ziane & Hadziioannou, 2019), or interactions with heterogeneous 3-D subsurface structure (Gualtieri et al., 2021).

The observed beampower (BP) maxima corresponding to retrograde Rayleigh waves during cyclones have on average higher values than those of the Love wavefield. This is true for both, the SM and PM frequency range. Love waves in the SM band generally show the lowest values, indicating weak/non-existent coherent wavefields or a relative abundance of uncorrelated Love wave noise in this frequency band. While this dominance of Rayleigh over Love waves is expected for the SM frequency range, it was also observed in the PM band, in contrast to previous studies that have presented evidence of dominant Love waves as well as high H/V ratios in the PM band (Friedrich et al., 1998; Becker et al., 2020). Our observation could be explained by the fact that seismic energy from SM sources with low frequencies (of about 0.08∼0.09 Hz) due to the high winds and the resulting long period SGWs might "leak" into the PM band defined here (0.05-0.09 Hz), contributing to increase the BP of PM Rayleigh waves. This energy leakage however seems to be more likely to occur the other way round, if we consider that dominant SGW with frequencies as low as $\sim$ 0.04Hz (half of 0.08Hz) are even for hurricanes relatively uncommon (and thus unlikely to generate strong SM signals), whereas the dominant SGW at higher frequencies ($f \gtrsim 0.1Hz$) may leak PM energy into the SM band considered here (0.10∼0.16 Hz). For examples of SGW spectra of hurricanes, see e.g. Knauss (1997); Ochi (2003) and Xu et al. (2014).

An alternative explanation for the observed dominance of Rayleigh BP values as in *e.g.* Fig. 6a is that cyclones are particularly efficient in exciting Rayleigh waves in the PM band. Such efficient Rayleigh over Love wave excitation could be site-dependent, as the maximum values occur only at well-defined backazimuths, even in the longer term, as depicted in Fig. 8. Under this assumption, the sporadic nature of cyclones and other major storms generating (the typically absent) Rayleigh waves in the PM band would explain the overall dominant PM Love waves reported in the literature, even if the latter were weak. The dominance of microseismic Rayleigh over Love waves in the SM band has been reported by e.g. Nishida et al. (2008) and Tanimoto et al. (2016). The latter studied a ring laser dataset spanning one whole year in Germany and found that SM Love waves are about 10 to 20 % stronger than Rayleigh during most of the year, while reporting the opposite during June and July (during which the hurricane season takes place). We are unaware of other observations of dominant Rayleigh over Love microseismic waves in the PM range. It is worth noting that comparing absolute BP values is however not fully objective since these partially depend on the added (and variable) S/N ratios of all stations over a given timespan, which can change in time *e.g.* if undesired background arrivals variably superpose in the frequency range of interest or if sensor coupling/sensitivity changes.

An additional observation is that the agreement of beamforming results between Rayleigh and Love waves in the same frequency band is often better relative to the agreement that there is for the same wave type between different frequency bands. The similarity is particularly obvious for Love and Rayleigh waves in the PM band, which suggests a coupled generation mechanism for both wave types in this frequency band. On the other hand, SM features tend to show stronger backazimuth variability of Love relative to Rayleigh waves, suggesting marked differences in the generation of each wave type in the SM band. A similar observation is outlined in Juretzek and Hadziioannou (2017). Alternatively, the higher variation in the SM frequency band may relate with high frequency PM leaking into the SM band, as explained above.

As indicated in Sec. 5, cyclone-related signals corresponding to stationary (fixed location) as well as non-stationary sources were identified. These signals are recognized during timespans with high wavefield coherency (high BP) and bearings that coincide with or consistently lag behind the backazimuths towards the hurricanes. While the stationary signal might only be apparent (as we only evaluate a single array), its recurrent backazimuth-invariability over long timespans is remarkable and contrasts with the changing bearing towards the hurricane tracks that triggered them.

The stable, stationary surface wave source located along the bearing towards Bermuda from the QC array was persistently highlighted as Gonzalo and Leslie crossed the region nearby (Figs. 3 and 4). The same backazimuth was also seen sporadically during all the other hurricanes studied (see Fig. S2 in the supporting material) and persistently during a full year (Fig. 8). The source region of this signal is discarded to be near the coast or shelf off the Gulf of Maine (which also lies along the same backazimuth great circle from QC array) since the waveheight observations in Figs. 3g,h and 4e,f are in better agreement with the region of Bermuda and additionally because the microseismic signal sets in just as Gonzalo crosses Bermuda on Oct 17 at noon (Figs. 3c-f and 4a-d). However, the exact location of this microseismic source region is not known. Based on the evidence, it is expected to lie somewhere in the Sargasso sea, around Bermuda, which is one of the very few oceanic islands located along the typical routes of Atlantic hurricanes (other than the Caribbean Antilles) and where geomorphological features such as seamounts and abrupt bathymetric changes are common. Further analyses are necessary to confidently explain the origin of such an efficient microseismic generation region at Bermuda, which we presume to be related to insular bathymetric features, geology and/or SGW regime around Bermuda, even though this region is not always clearly highlighted in the hindcast data.

Strong sources are observed as hurricanes approach the shallow-water regions over the continental platform. This was observed during the landfall of Florence; the re-entry of Michael into the Atlantic; or on Oct 16 during Nicole, in which a prominent signal was seen as its track approached the protruding edge of the continental slope (Fig. S2). The non-stationary microseisms observed during the approach of hurricanes Gonzalo and Leslie to the Great Banks of Newfoundland and its continental slope also support this observation and were confirmed via P-wave ray tracing (not shown).

Fan et al. (2019) studied Z-component records in the band 0.02-0.05 Hz (below the PM band) and reported similar microseisms source areas at the Great Banks of Newfoundland parallel to the shelf break offshore Nova Scotia in front of the Saint-Lawrence river bay during hurricane Gonzalo in both its rear quadrants on Oct 19th 2014 (a C1 hurricane at the time), between 6:00-9:00am (compare Figs. 7b,d with supporting Fig. S3, which includes a modified version of the original Fig. 3e in Fan et al., 2019). These microseisms roughly match the here observed Rayleigh and Love wave BP peaks in both the PM and SM bands occurring in the same region and same times (Figs. 3d,f and 4b,d). It is worth noting that these kind of signals were not detected as Gonzalo had a higher category (> 2) but was farther away from the QC array. In Fan et al. (2019), the traced sources also do not occur where the maximum waveheights are, but rather in the rear

quadrants of Gonzalo as well as outside of the main wind influence area, slightly more numerous to the left of the path (in the movement direction), around an area in which a gradient of wave heights exists and where the main wave direction was perpendicular to the shelf line (Fig. S3a). The sources there seem to be primarily controlled by the shape of the shelf break instead of the shape of the waveheight anomaly.

In our study, signals related to Gonzalo continue to exist further north up to the coast off Newfoundland, entering Labrador Sea, all along the continental platform, but it is unclear if these are generated along the continental slope break or underneath the track (over the flat continental shelf). The discontinuity and slight decrease in BP values observed for SM Rayleigh and Love waves during Gonzalo on Oct 19 at 12:00 (4b,d) coincides with the translation of the microseismic source area from the shelf break onto the continental platform. Rayleigh waves continue to be clearly detected afterwards, while Love waves become somewhat scattered and weak. This suggests that SM Love waves are amplified mostly along the inclined shelf slope, probably due to the rugged relief and/or complex layering structures, which are thought to be efficient generators of Love and converted waves (e.g. Tanimoto et al., 2016; Nishida, 2017; Ziane & Hadziioannou, 2019; Le Pape et al., 2021). At the same time, prominent PM signals for both Rayleigh and Love waves appear as the source area moves into the continental slope (Figs. 3d,f), as expected from the shallow generation of PM. The potential use of microseisms for imaging of shallow sedimentary layers is thus evoked. We detected no signal that was actively generated over the flat deep ocean.

For non-stationary signals, we observed that they generally trail the eye of the hurricane (*e.g.* Figs. 3 and 4). This means that the source lies in the rear quadrants of the hurricane or along its wake. This observation of microseisms linked to the trail of storms was also reported by Chevrot et al. (2007); Chi et al. (2010) and Zhang et al. (2010). Similar results were also found by Farra et al. (2016) and Lin et al. (2017), who observed microseismic sources in the left rear quadrant of a Northern hemisphere typhoon, where crossing seas occur, and up to 200 km behind the eye (Davy et al., 2014). Interestingly, the highest wave heights occur in the right (left) quadrant of hurricanes in the Northern (Southern) hemisphere, where wind speed and cyclone speed vectors align constructively, so that the highest waves do not necessarily determine microseismic excitation, as also suggested by Fig. 7. Park and Hong (2020) found persistent delays of 6h or more between activation of a microseismic source area and the passage of the eye of the typhoon over the respective area, in accordance with our observations. Altogether, the idea of a forcing region of microseisms "behind" storms was suggested by Tabulevich (1971) and is implicit as well in the class IIIa source mechanism of SM (see Ardhuin, Stutzmann, Schimmel, & Mangeney, 2011), suggested originally by Longuet-Higgins (1950), in which the backwards propagating wind waves at the wake of a storm interact with the forward swells generated in previous times if the system moves fast enough. Interestingly, the observed PM signals for the hurricanes show the same spatial delay as the SM signals. For PM frequency band Rayleigh waves this might be explained by leaking of SM mechanisms with low frequencies into the PM frequency band or would alternatively suggest that the non-linear SGW self-interaction mechanism (or the interaction with reflected SGW or distant swells) might not be necessary to explain the trailing SM signals. In any case, a strong site control agrees with the uniformity of the beamforming results for all wave types in the entire microseismic band.

Our results reveal that cyclone-generated microseismic surface waves can be generated in shallow bathymetry (*i.e.* the continental shelf, rise or regions around islands) not exclusively linked to coasts. Microseisms generation in shallow bathymetry was also observed by e.g. Essen et al. (2003); Bromirski et al. (2013); Ying et al. (2014). Guo et al. (2020) studied Rayleigh waves in the eastern North American margin and found that PMs (0.050 to 0.085 Hz) are likely distributed along the continental shelf and adjacent deep ocean areas (in this study these seem strongly related to shallow waters too), while

the long-period SM (0.1 to 0.2 Hz – attributed to distant swells) occurs in deep ocean regions near the continental slope, in agreement with our results. In contrast, other authors argue for deep ocean microseisms (e.g. Zhang et al., 2010; Gualtieri et al., 2015). Based on our results, the existence of coherent, deep-ocean-generated microseismic signals strong enough to be detected inland cannot be ruled out neither be supported. As an example, very little microseismic energy was detected as hurricane Lorenzo (the farthest away from QC array) moved along the mid-Atlantic ridge (Fig. 1). It would be interesting to confirm if microseismic generation over this region is actually possible, as the water depths are comparable to those of the shelf break sections in which microseisms were readily detected. If strong, deep water microseismic signals do exist, evidence would suggest that attenuation makes them virtually invisible to arrays located as far as 4000 km away. As a reference, Ebeling (2012) cites 2000 km as the threshold distance for cyclone microseism detection, while Davy et al. (2014) shows with OBS stations that at distances of more than 1300 km the microseisms generated by a C1 cyclone are less than $\sim 10\%$ their source amplitudes.

The oceanic regions with largest mean waveheights or F_{p3D} values during each hurricane were not always highlighted by prominent BP maxima, which in turn often pointed towards regions with low oceanic anomalies, if present at all (see Fig. 7). Added to water depth, further physical parameters that combine with the SGW forcing might play a relevant role in the observed microseismic signals. Candidates include: seabed morphology at wavelength scale; subsurface lithology and structure; oceanic mesoscale phenomena and structure, or other factors not yet considered. As a way of example, Sepúlveda et al. (2005), Rodgers et al. (2010), Khan et al. (2020), amongst others, outline how surface wave (de-)focusing can occur due to reflections in topography such as ridges and mountain tops, being a possible contributing factor for microseisms amplification at the continental break.

7 Conclusions

Cyclones wandering over the ocean generate distinctive microseismic waves that can be detected at land stations. These microseisms occur for both retrograde Rayleigh and Love waves in the microseismic frequency band, from about 0.05 to 0.2 Hz. A significant observation is that these signals are not excited equally during the entire lifetime of the cyclone but instead intermittently as semi-continuous pulses at specific oceanic locations as the cyclones are passing by, hampering a continuous cyclone-tracking via far-field arrays.

Apart from differences in BP levels and distribution of maxima, cyclone-related Love and Rayleigh wave sequences tend to occur simultaneously and roughly match each other in direction of arrival quite well in most scenarios, particularly in the same frequency band, suggesting a colocation of the generation area and a strong local (site) control. However, Love wave radiation is more diffuse and less coherent or weaker, while the generation of Rayleigh waves is more coherent and focused. The sharpest and most accurate cyclone trackings were obtained for Rayleigh waves in both the primary (PM) and secondary (SM) frequency band. Both wave types were most efficiently excited at fixed shallow regions including the continental slope and shallow shelf off Newfoundland and possibly a region surrounding the island of Bermuda, virtually independently of storm category. No cyclone microseisms were safely linked to deep open ocean regions.

Two types of cyclone-related signals were identified: non-stationary and stationary. The former appear to occur at the trail of cyclones, often shifted more than 500 km off the *eye*, suggesting that wind waves in the rear quadrants and cyclone-originated swells play a significant role in the microseismic generation, likely providing an optimum surface gravity wave (SGW) directional spectrum. Occasionally, the passage of cyclones over or nearby oceanic regions where microseismic generation is highly efficient triggers strong

stationary signals that can last several days. Moreover, the power spectral density (PSD) of the SGW pressure fluctuation generated by non-linear wave-wave interactions and the bathymetry alone seem insufficient to reliably predict regions where the strongest cyclone microseisms are excited.

Major advances in the field of microseisms have been published, yet the complex interplay between site factors such as seabed morphology, near-bottom geology and structure and the SGW spectrum forcing is not fully understood. On the other hand, the existence of prominent microseisms related to cyclones at well-defined oceanic regions and their strong dependence on the aforementioned site properties is inviting for passive imaging and monitoring, in particular considering that forecasts of the tracks of cyclones are pre-available via accurate meteorological models. Such goals would significantly benefit of near-field (on- and off-shore) observations using OBS, floating seismographs (e.g. MERMAIDS - see Hello & Nolet, 2020), or dense, optimal and widespread sensor layouts such as large-N-arrays or DAS. An improved detection and understanding of oceanic microseisms has the potential to refine the existing atmosphere-ocean-solid earth coupled models.

Acronyms

ARF Array response (transfer) function
BP Beampower
DF Double frequency (related to non-linear interactions of surface gravity waves travelling in opposite directions)
DAS Distributed Acoustic Sensing
OBS Ocean-bottom seismometer(s)
PM Primary Microseism(ic)
PSD Power spectral density
QC Reference to the virtual array in Québec, Canada implemented in this study
SGW Surface gravity wave(s)
SM Secondary Microseism(ic)
ROCI Radius of outermost closed isobar of a cyclone
WWSSN World-Wide Standardized Seismograph Network

Open Research

The Atlantic cyclone data was obtained from `http://ibtracs.unca.edu/` (Knapp K.R., Applequist, S., Diamond, H.J., Kossin, J.P., Kruk, M., and Schreck, C. (2010). NCDC International Best Track Archive for Climate Stewardship (IBTrACS) Project, Version 3. 2010-2019 catalogue. NOAA National Centers for Environmental Information. DOI:10.7289/V5NK3BZP. last accesed on march 2021). The seismic data was recorded by seismometers of the Canadian National Seismic Network (`https://www.fdsn.org/networks/detail/CN/`) and was freely accessed through the IRIS client (`http://ds.iris.edu/ds/`) of the International Federation of Digital Seismograph Networks server (`https://www.fdsn.org/`). Stations for the virtual array were selected using the wilber3 tool of the IRIS consortium (`http://ds.iris.edu/wilber3/find$\_$event`). Hindcast data was downloaded from the French Research Institute for Exploitation of the Sea (IFREMER, `https://wwz.ifremer.fr/`) at `ftp://ftp.ifremer.fr/ifremer/ww3/HINDCAST`, and bathymetry from GEBCO (`https://www.gebco.net/`). The 3C-Beamforming script was mainly developed by Carina Juretzek. The data downloading, pre-processing, processing and plotting of results relied mainly on Obspy ("ObsPy: a python toolbox for seismology, author=Beyreuther, M and Barsch, R and Krischer, L and Megies, T and Behr, Y and Wassermann, J", 2010), a Python-based seismological data management module (`https://docs.obspy.org/`https://docs.obspy.org/).

Several other standard libraries and modules for scientific computing were implemented (*e.g.* Numpy, Scipy, Matplotlib, Cartopy, Colorcet and Cmocean).

Acknowledgments

This work was partially funded by the Emmy Noether program (HA7019/1-1) of the German Research Foundation (DFG). J.D. Pelaez Quiñones would like to thank the authors of all the previous works upon which ours was based and the corresponding sources that made them available.

References

Ardhuin, F., Gualtieri, L., & Stutzmann, E. (2015). How ocean waves rock the Earth: Two mechanisms explain microseisms with periods 3 to 300 s. , *42 (3)*, 765–772.

Ardhuin, F., Stutzmann, E., Schimmel, M., & Mangeney, A. (2011). Ocean wave sources of seismic noise. *J. Geophys. Res.*, *116*, C09004.

Becker, D., Cristiano, L., Peikert, J., Kruse, T., Dethof, F., Hadziioannou, C., & Meier, T. (2020). Temporal Modulation of the Local Microseism in the North Sea. *J. Geophys. Res.: Solid Earth*, *125*(10), e2020JB019770.

Bowen, S., Richard, J., Mancini, J., Fessatidis, V., & Crooker, B. (2003). Microseism and infrasound generation by cyclones. *Journal of the Acoustical Society of America*, *113(5)*, 2562–2573.

Bromirski, P., & Duennebier, F. (2002). The near-coastal microseism spectrum: Spatial and temporal wave climate relationships. *J. Geophys. Res.*, *107*(B8), 2166-85.

Bromirski, P., Stephen, R., & Gerstoft, P. (2013). Are deep-ocean-generated surface-wave microseisms observed on land? *J. Geophys. Res.: Solid Earth*, *118 (B10)*, 3610-3629.

Cessaro, R. (1994). Sources of Primary and Secondary Microseisms. *Bull. Seismo. Soc. Amer.*, *84-1*, 142-148.

Cessaro, R., & Chan, W. (1989). Wide-angle triangulation array study of simultaneous primary microseism sources. *J. Geophys. Res.*, *94 (B11)*, 15,555.-15,563.

Chen, S., & Curcic, M. (2015). Ocean surface waves in Hurricane Ike (2008) and Superstorm Sandy (2012): Coupled model predictions and observations. *Ocean Modelling*, *000*, 1-16.

Chevrot, S., Sylvander, M., Benahmed, S., Ponsolles, C., Lefevre, J., & Paradis, D. (2007). Source locations of secondary microseisms in western Europe: Evidence for both coastal and pelagic sources. *J. Geophys. Res.*, *112*, B11301.

Chi, W., Chen, W., Kuo, B., & Dolenc, D. (2010). Seismic monitoring of western Pacific typhoons. *Mar. Geophys. Res.*, *31*, 239-251.

Davy, C., Barruol, G., Fontaine, F., Sigloch, K., & Stutzmann, E. (2014). Tracking major storms from microseismic and hydroacoustic observations on the seafloor. *Geophys. Res. Letters*, *41*, 8825-8831.

Ebeling, C. (2012). Inferring Ocean Storm Characteristics from Ambient Seismic Noise: A Historical Perspective. *Advanc. in Geophys.*, *53*, 1-28.

Emanuel, K. (2017a). Assessing the present and future probability of Hurricane Harvey's rainfall. In *Proceedings of the national academy of sciences.*

Emanuel, K. (2017b). Will Global Warming Make Hurricane Forecasting More Difficult? *Bulletin of the American Meteor. Society*, *98*, 495-501.

Esmersoy, C., Cormier, V., & Toksöz, M. (1985). *Three-Component Array Processing* (Tech. Rep.). The VELA Program: A Twenty-five Year Review of Basic Research.

Esquivel-Trava, B., Ocampo-Torres, F., & Osuna, P. (2015). Spatial structure of directional wave spectra in hurricanes. *Ocean Dynamics*, *65*, 55-76.

Essen, H., Krüger, F., Dahm, T., & Grevemeyer, I. (2003). On the generation of secondary microseisms observed in northern and central Europe. *J. Geophys. Res.*, *108 (B10)*, 2506.

Fan, W., McGuire, J., de Groot-Hedlin, C., Hedlin, M., Coats, S., & Fiedler, J. (2019). Stormquakes. *Geophys. Res. Letters*, *46, Issue 22*, 12909-12918.

Farra, V., Stutzmann, E., Gualtieri, L., Schimmel, M., & Ardhuin, F. (2016). Ray-theoretical modeling of secondary microseism P waves. *Geophys. J. Int.*, *206*, 1730-1739.

Friedrich, A., Klinge, K., & Krueger, F. (1998). Ocean-generated microseismic noise located with the Graefenberg array. *J. Seismol.*, *2(1)*, 47-64.

Fukao, Y., Nishida, K., & Kobayashi, N. (2010). Seafloor topography, ocean infragravity waves, and background Love and Rayleigh waves. *J. Geophys. Res.*, *115*, B04302.

Gal, M., Reading, A., Ellingsen, S., Koper, K., & Burlacu, R. (2017). Full wavefield decomposition of high-frequency secondary microseisms reveals distinct arrival azimuths for Rayleigh and Love waves. *J. Geophys. Res.: Solid Earth*, *122*, 4660-4675.

Gerstoft, P., Fehler, M., & Sabra, K. (2006). When Katrina hit California. *Geophys. Res. Letters*, *33*, L17308.

Gilmore, M. (1947). Tracking ocean storms with the seismograph. *Bulletin of the American Meteor. Society*, *28*, 73-86.

Gualtieri, L., Bachmann, E., Simons, F. J., & Tromp, J. (2021). Generation of secondary microseism Love waves: effects of bathymetry, 3-D structure and source seasonality. *Geophys. J. Int.*, *226*(1), 192-219.

Gualtieri, L., Stutzmann, E., Capdeville, Y., Farra, V., Mangeney, A., & Morelli, A. (2015). On the shaping factors of the secondary microseismic wavefield. *J. Geophys. Res.: Solid Earth*, *120*, 6241-6262.

Guo, Z., Xue, M., Aydin, A., & Ma, Z. (2020). Exploring source regions of single- and double-frequency microseisms recorded in eastern North American margin (ENAM) by cross-correlation. *Geophys. J. Int.*, *220*, 1352-1367.

Gutenberg, B. (1936). On microseisms. *Bull. Seismo. Soc. Amer.*, *26 (2)*, 111-117.

Gutenberg, B. (1958). Microseisms. *Advanc. in Geophys.*, *5*, 53-92.

Hadziioannou, C., Gaebler, P., Schreiber, U., Wassermann, J., & Igel, H. (2012). Examining ambient noise using colocated measurements of rotational and translational motion. *J. Seismol.*, *16*, 787-796.

Hasselmann, K. (1963). On the non-linear energy transfer in a gravity-wave spectrum, Part 2. Conservation theorems; wave particle analogy; irreversibility. , *15*, 273-281.

Hello, Y., & Nolet, G. (2020). "Floating Seismographs (MERMAIDS)". In H. K. Gupta (Ed.), *Encyclopedia of solid earth geophysics* (pp. 1–6). Cham: Springer International Publishing.

Hu, K., & Chen, Q. (2011). Directional spectra of hurricane-generated waves in the Gulf of Mexico. *Geophys. Res. Letters*, *38*, L19608.

Juretzek, C., & Hadziioannou, C. (2016). Where do ocean microseisms come from? A study of Love-to-Rayleigh wave ratios. *J. Geophys. Res.: Solid Earth*, *121*(9), 6741–6756.

Juretzek, C., & Hadziioannou, C. (2017). Linking source region and ocean wave parameters with the observed primary microseismic noise. *Geophys. J. Int.*, *211*(3), 1640–1654.

Kedar, S., Longuet-Higgins, M., Webb, F., Graham, N., Clayton, R., & Jones, C. (2008). The origin of deep ocean microseisms in the North Atlantic Ocean. *Proc. R. Soc. A*, *464*, 777-794.

Khan, S., van der Meijde, M., van der Werff, H., & Shafique, M. (2020). The impact of topography on seismic amplification during the 2005 Kashmir earthquake. *Nat. Hazards Earth Syst. Sci.*, *20*, 399-411.

Kibblewhite, A., & Wu, C. (Eds.). (1996). *Wave Interactions as seismo-acustic source*. Berlin Heidelberg: Springer.

Knapp, K., Kruk, M., Levinson, D., Diamond, H., & Neumann, C. (2010). The International Best Track Archive for Climate Stewardship (IBTrACS): Unifying tropical cyclone best track data. *Bulletin of the American Meteor. Society*, *91*, 363-376.

Knauss, J. (1997). *Introduction to physical oceanography. 2nd edition.* Long Grove, Illinois: Waveland Press, Inc.

Kossin, J., Emanuel, K., & Vecchi, G. (2014). The poleward migration of the location of tropical cyclone maximum intensity. *Nature*, *509*, 349-356.

Kossin, J., Knapp, K., Olander, T., & Velden, C. (2020). Global increase in major tropical cyclone exceedance probability over the past four decades. In *Proceedings of the national academy of sciences.*

Landès, M., Hubans, F., Shapiro, N., Paul, A., & Campillo, M. (2010). Origin of deep ocean microseisms by using teleseismic body waves. *J. Geophys. Res.*, *115*, B05302.

Le Pape, F., Craig, D., & Bean, C. J. (2021). How deep ocean-land coupling controls the generation of secondary microseism Love waves. *Nature Communications*, *12:2332*, 2562–2573.

Lin, J., Lin, J., & Xu, M. (2017). Microseisms Generated by Super Typhoon Megi in the Western Pacific Ocean. *J. Geophys. Res.: Oceans*, *122*, 1-12.

Longuet-Higgins, M. (1950). A theory of the origin of microseisms. *Phil. Trans. Roy. Soc.*, *243*, 1-35.

Löer, K., Riahi, N., & Saenger, E. H. (2018, 02). Three-component ambient noise beamforming in the Parkfield area. *Geophys. J. Int.*, *213*(3), 1478-1491.

Matsuzawa, T., Obara, K., Maeda, T., Asano, Y., & Saito, T. (2012). Love- and Rayleigh-Wave Microseisms Excited by Migrating Ocean Swells in the North Atlantic Detected in Japan and Germany. *Bull. Seismo. Soc. Amer.*, *102 (4)*, 1864-1871.

Meschede, M., Stutzmann, E., Farra, V., Schimmel, M., & Ardhuin, F. (2017). The Effect of Water Column Resonance on the Spectra of Secondary Microseism P Waves. *J. Geophys. Res.: Solid Earth*, *122*, 8121-8142.

Nakata, N., Gualtieri, L., & Fichtner, A. (Eds.). (2019). *Seismic Ambient Noise.* Cambridge: Cambridge University Press.

Nishida, K. (2017). Ambient seismic wave field. *Proc. Jpn. Acad., Ser. B*, *93 (7)*, 423-448.

Nishida, K., Kawakatsu, H., Fukao, Y., & Obara, K. (2008). Background Love and Rayleigh waves simultaneously generated at the Pacific Ocean floors. *Geophys. Res. Letters*, *35*(16).

ObsPy: a python toolbox for seismology, author=Beyreuther, M and Barsch, R and Krischer, L and Megies, T and Behr, Y and Wassermann, J. (2010). *Seismol. Res. Lett.*, *81(3)*, 530-533.

Ochi, M. (2003). *Hurricane-generated seas. 1st edition.* Oxford: Elsevier.

Park, S., & Hong, T. (2020). Typhoon-Induced Microseisms around the South China Sea. *Seismol. Res. Lett.*, *XX*, 1-15.

Retailleau, L., & Gualtieri, L. (2019). Toward High-Resolution Period-Dependent Seismic Monitoring of Tropical Cyclones. *Geophys. Res. Letters*, *46*, 1-9.

Retailleau, L., & Gualtieri, L. (2021). Multi-phase seismic source imprint of tropical cyclones. *Nature Communications*, *12(1)*(2064).

Rodgers, A., Petersson, N., & Sjogreen, B. (2010). Simulation of topographic effects on seismic waves from shallow explosions near the North Korean nuclear test site with emphasis on shear wave generation. *J. Geophys. Res.*, *115*, B11309.

Saito, T. (2010). Love-wave excitation due to the interaction between a propagating ocean wave and the sea-bottom topography. *Geophys. J. Int.*, *182 (3)*, 1515-1523.

Sepúlveda, S., Murphy, W., Jibson, R., & Petley, D. (2005). Seismically induced rock slope failures resulting from topographic amplification of strong ground motions: The case of Pacoima Canyon, California. *Engineering Geology*, *80*, 336-348.

Stutzmann, E., Ardhuin, F., Schimmel, M., Mangeney, A., & Patau, G. (2012). Modelling long-term seismic noise in various environments. *Geophys. J. Int.*, *191(2)*, 707-722.

Sutton, G., & Barstow, N. (1996). Ocean bottom microseisms from a distant super-typhoon. *Geophys. Res. Letters*, *23, 5*, 499-502.

Tabulevich, V. (1971). The effect of the velocity of the centre of a cyclone on the generation of microseisms. *Pure Appl. Geophys.*, *85*, 69-74.

Tanimoto, T. (2013). Excitation of microseisms: Views from the normal-mode approach. *Geophys. J. Int.*, *194*, 1755-1759.

Tanimoto, T., Hadziioannou, C., Igel, H., Wassermann, J., Schreiber, U., Gebauer, A., & Chow, B. (2016). Seasonal variations in the Rayleigh-to-Love wave ratio in the secondary microseism from colocated ring laser and seismograph. *J. Geophys. Res.: Solid Earth*, *121*, 2447-2459.

Tanimoto, T., & Valovcin, A. (2015). Stochastic excitation of seismic waves by a hurricane. *J. Geophys. Res.: Solid Earth*, *120*, 7713-7728.

Traer, T., Gerstoft, P., Bromirski, P., & Shearer, P. (2012). Microseisms and hum from ocean surface gravity waves. *J. Geophys. Res.*, *117*, B11307.

Wallace, J., & Hobbs, P. (2006). *Atmospheric Science - An introductory survey. 2nd edition.* Elsevier.

Ward Neale, J., Harmon, N., & Srokosz, M. (2018). Improving microseismic P wave source location with multiple seismic arrays. *J. Geophys. Res.: Solid Earth*, *123*.

Xu, F., Bhui Thi, T., & Perrie, W. (2014). The observed analysis on the wave spectra of Hurricane Juan. *Acta Oceanol. Sin.*, *33 (11)*, 112-122.

Ying, Y., Bean, C., & Bromirski, P. (2014). Propagation of microseisms from the deep ocean to land. *Geophys. Res. Letters*, *41*, 6374-6379.

Young, I. (1998). Observations of the spectra of hurricane generated waves. *Ocean Engng*, *25 (4-5)*, 261-276.

Young, I. (2006). Directional spectra of hurricane wind waves. *J. Geophys. Res.*, *111*, C08020.

Zhang, J., Gerstoft, P., & Bromirski, P. (2010). Pelagic and coastal sources of P-wave microseisms: Generation under tropical cyclones. *Geophys. Res. Letters*, *37*, L15301.

Ziane, D., & Hadziioannou, C. (2019). The contribution of multiple scattering to Love wave generation in the secondary microseism. *Geophys. J. Int.*, *217*, 1108-1122.